ACS Photonics
Article
pubs.acs.org/journal/apchd5

Electrical Switching of Infrared Light Using Graphene Integration with Plasmonic Fano Resonant Metasurfaces

Nima Dabidian,[†] Iskandar Kholmanov,[‡,§] Alexander B. Khanikaev,[∥,⊥] Kaya Tatar,[†] Simeon Trendafilov,[†] S. Hossein Mousavi,[†] Carl Magnuson,[‡] Rodney S. Ruoff,[‡] and Gennady Shvets*[,†]

Departments of [†]Physics and Center for Nano and Molecular Science and Technology and [‡]Mechanical Engineering and Materials Science Program, The University of Texas at Austin, Austin, Texas 78712, United States
[∥]Department of Physics, Queens College of The City University of New York, Queens, New York 11367, United States
[⊥]The Graduate Center of The City University of New York, New York, New York 10016, United States
[§]CNR-INO, Sensor Lab, The University of Brescia, via Branze 45, 25123, Brescia, Italy

Ⓢ *Supporting Information*

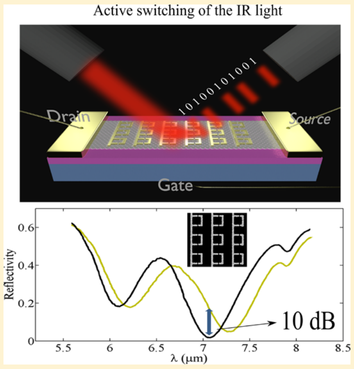

ABSTRACT: Graphene has emerged as a promising optoelectronic material because its optical properties can be rapidly and dramatically changed using electric gating. Graphene's weak optical response, especially in the infrared part of the spectrum, remains the key challenge to developing practical graphene-based optical devices such as modulators, infrared detectors, and tunable reflect-arrays. Here it is experimentally and theoretically demonstrated that a plasmonic metasurface with two Fano resonances can dramatically enhance the interaction of infrared light with single layer graphene. Graphene's plasmonic response in the Pauli blocking regime is shown to cause strong spectral shifts of the Fano resonances without inducing additional nonradiative losses. It is shown that such electrically controllable spectral shift, combined with the narrow spectral width of the metasurface's Fano resonances, enables reflectivity modulation by nearly an order of magnitude. We also demonstrate that metasurface-based enhancement of the interaction between graphene and infrared light can be utilized to extract one of the key optical parameters of graphene: the free carrier scattering rate. Numerical simulations demonstrate the possibility of strong active modulation of the phase of the reflected light while keeping the reflectivity nearly constant, thereby paving the way to tunable infrared lenses and beam steering devices based on electrically controlled graphene integrated with resonant metasurfaces.

KEYWORDS: *optical switching, Fano resonance metasurface, graphene, modulation depth*

An optical metasurface[1,2] is a two-dimensional (single-layer) metamaterial which lends itself to much easier fabrication compared with its fully three-dimensional (3D) counterpart. Plasmonic metasurfaces are already finding applications in a variety of areas such as light manipulation,[3−10] biochemical sensing,[10−12] nonlinear optics,[13,14] and spectrally selective thermal emission,[15] to name just a few. Ultrathin optical components such as optical lenses,[16,17] wave-plates,[18] and beam steering devices[3,19] are some of the recent examples of employing metasurfaces for molding the flow of light. The scalability and universality of the metasurface design enables their deployment across the entire electromagnetic spectrum. Especially attractive are the metasurfaces designed to operate in the mid-infrared (mid-IR) part of the optical spectrum. That is due to two factors: the variety of technological applications and the limited choice of conventional optical components in the mid-IR spectral region. For example, the 2−20 μm spectral range hosts important biomolecular and chemical fingerprints that are being exploited for ultrasensitive fingerprinting and characterization of molecular monolayers.[9,12] In addition, the atmospheric transparency windows of 3−5 μm and 8−12 μm are exploited for a variety of thermal imaging applications.[20,21] These unique properties of infrared radiation are now used to address crucial health, security, and environmental applications,[9,22−25] but more rapid progress is impeded by the limited availability of passive and active mid-infrared devices and components such as sources and detectors,[26−30] as well as optical modulators and switches.[31−38]

This niche can be potentially filled by active plasmonic metasurfaces. For example, plasmonic enhancement of light-matter interaction improves the performance and reduces the sizes of detectors,[39−41] sensors,[42−44] and lasers.[45] When integrated with electrically or mechanically tunable materials or substrates, plasmonic metasurfaces can assume the role of a versatile platform for developing dynamically tunable optical devices, thus, paving the way for a variety of technological applications in hyper-spectral imaging,[46] single pixel detection,[47] and 3D imaging,[48] Such devices could potentially overcome some of the limitations (e.g., slow response time, shallow

Received: September 5, 2014
Published: December 22, 2014

DOI: 10.1021/ph5003279
ACS Photonics 2015, 2, 216−227

modulation depth, and narrow bandwidth) of the existing platforms for IR light modulators that utilize liquid crystals,[31,32] advanced materials exhibiting metal–insulator phase transitions,[33] mechanically stretchable elastomeric materials, or semiconductor interfaces controlled through electrostatic carrier depletion.[35,38] Here we experimentally demonstrate that these limitations can be potentially overcome by integrating spectrally selective plasmonic metasurfaces with single-layer graphene (SLG). The proposed graphene-metasurface modulator of free-space infrared beams works in either transmission or reflection, and possesses a relatively large (several percent) spectral bandwidth. Ultrafast response time is accomplished due to rapid injection of charge carriers into SLG while large modulation depth (about 10 dB) in reflection is achieved by the metasurface design.

SLG is a promising material for light modulation because its optical conductivity can be tuned by electrostatic or chemical doping. This property has already been utilized to tune the IR absorption and spectral response of plasmonic metasurfaces,[49−53] and it has been shown that the carrier density in SLG can be potentially modulated at tens of MHz rate.[51,54,55] Despite encouraging theoretical predictions,[54,56] a modulation depth above 30%[51] in the mid-IR has never been experimentally demonstrated so far. The limited effect of the SLG on plasmonic metasurfaces in mid-IR is due to two factors: (i) relatively broad plasmonic resonances in that spectral range,[57] and (ii) weak absorption of graphene in mid-IR due to the absence of interband transitions.[50] Small modulation depth of the reflected IR radiation produced by electric gating of the SLG puts into question its very viability as an active material for future optical modulators that have much more stringent performance requirements, such as tens of decibels (dBs) maximum-to-minimum signal variation.

In this work we experimentally demonstrate that, by integrating an SLG with a high-Q Fano-resonant metasurface, it is possible to modulate mid-IR reflectivity by an order of magnitude ($\approx$ 10 dB), thus achieving the modulation depth as high as 90% using electrostatic gating. This is accomplished by designing a metasurface that exhibits a spectrally narrow reflectivity dip. The strong enhancement of the electric field component parallel to the SLG's surface is shown to result in strong graphene/metasurface coupling that inductively[50] (i.e., essentially losslessly) shifts the plasmonic resonances of the metasurface by approximately half of the spectral width. The resulting electrically controlled deep modulation of the reflected IR light is caused by the said spectral shift which is determined by graphene's optical conductivity $\sigma_i(n)$ and controlled by varying the charged carriers' concentration $n(V_g)$ in the SLG by applying a variable back-gate voltage V_g.

We also use first-principles electromagnetic simulations to demonstrate that the phase and amplitude of the reflected light can be dynamically varied independently of each other. Phase modulation (PM) at the specific wavelength λ_R^{PM} can be accomplished by keeping the amplitude R of the reflected light constant while varying its phase ϕ_R as a function of V_g. Similarly, amplitude modulation (AM) can be accomplished at the specific wavelength λ_R^{AM}. Similar amplitude and phase modulation can be accomplished in transmission, thus paving the way for infrared rapidly tunable reflect- and transmit-arrays. The effects of graphene's strong coupling to the metasurface on the optical response (i.e., the wavelength-dependent reflectivity/phase and the line width of the reflectivity peak) are investigated by varying the charged carriers' concentration in the electrically gated SLG.

Finally, we experimentally demonstrate the possibility of all-optical measurement of the free carrier collisional time τ in electrically gated graphene coupled to a Fano-resonant metasurface. A simple procedure for extracting τ from the reflectivity spectra of the integrated graphene/plasmonic metasurface is described. This procedure is valid in the low optical frequency regime, where graphene's optical conductivity is dominated by graphene's Drude response. It is demonstrated that thus extracted carrier scattering time is consistent with that obtained using dc conductivity measurements.

■ RESULTS AND DISCUSSION

Because the main motivation of this work is the development of an efficient electrically controlled IR modulator, we start by reviewing the desired properties of such device. A conceptual example of a reflection modulator is shown in Figure 1a, where the wavelength-dependent reflectivity $R(\lambda)$ from a frequency-selective metasurface can be spectrally shifted from the on- to the off-state by some nonoptical (e.g., electrical) means. Ideally, at the targeted wavelength λ, such modulator would have a relatively high on-reflectivity $R_{on}(\lambda)$ and very low off-reflectivity $R_{off}(\lambda)$ in its off-state. The spectral shift could be caused, for example, by applying back-gate voltage V_g to the layer of graphene as shown in Figure 1b. The performance of such modulator would be characterized by the modulation depth (MD) defined as MD $\equiv (1 - R_{off}/R_{on}) \times 100\%$. A high-performing modulator must have MD > 90%.

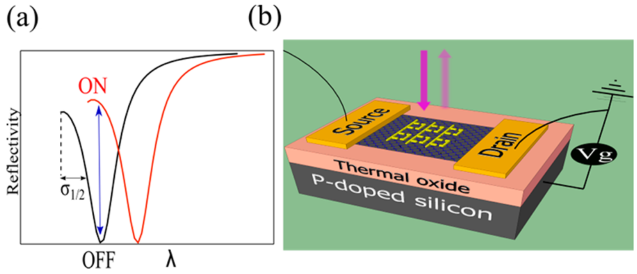

Figure 1. (a) Conceptual schematic of an efficient light modulator based on a frequency-selective tunable reflector. Key features: narrow line width, large spectral shift, and zero reflectivity at the targeted wavelength. The HWHM of the reflectivity peak ($\sigma_{1/2}$) is shown by the black arrow. (b) The realization based on a Fano-resonant metasurface integrated with graphene. Spectral shifting is achieved by back-gating of the graphene underneath the metasurface.

It follows from Figure 1a that the metasurface and its reflectivity $R(\lambda)$ must satisfy the following requirements: (a) narrow line width $\sigma_{1/2}$ that can be bridged by graphene-induced spectral shift $\Delta\lambda$; (b) strong concentration of the optical energy by the metasurface capable of producing $\Delta\lambda \sim \sigma_{1/2}$; and (c) near-zero reflectivity in the vicinity of the target wavelength λ. To satisfy these conditions, we have designed a metasurface which exhibits broadband reflectivity that is greatly reduced at the two nearby wavelengths due to the phenomenon of plasmon-induced electromagnetically induced transparency (EIT),[58,59,4] which is directly related to[66] Fano interference.

Computational Design of the Metasurface. The schematic unit cell and the SEM image of the fabricated metasurface are shown in Figure 2a,b. The unit cell consists of three key elements: (i) a metallic wire that electrically connects the neighboring cells in y-direction, and whose functionality is to provide broadband reflectivity of the y- polarized light; (ii) a pair

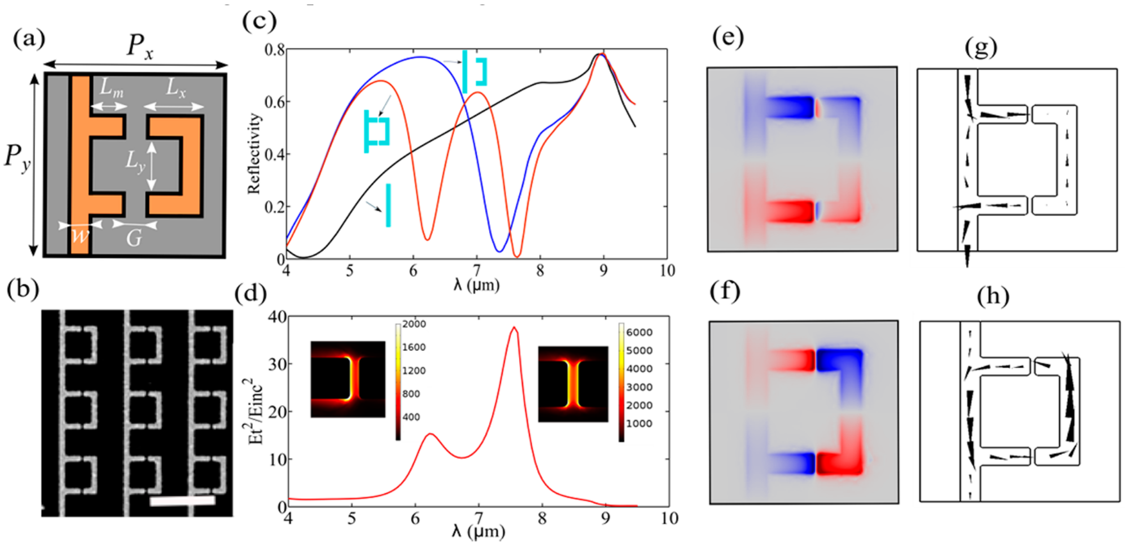

Figure 2. Design of a metasurface exhibiting double-Fano resonance. (a) Geometry of the unit-cell of the metasurface with parameters: $P_x = P_y = 3$ μm, $L_x = 0.675$ μm, $L_m = 0.75$ μm, $L_y = 1.2$ μm, and $w = 0.3$ μm. Gap sizes are $G = 70$ nm for sample 1 (shown here) and $G = 100$ nm for sample 2. Metal thickness for both samples: $t_m = 30$ nm (5 nm Cr + 25 nm gold). (b) SEM image of the metasurface fabricated on top of graphene. Scale bar: 3 μm. (c) Simulated reflectivity of normally incident y-polarized light for wire grid (black), wire, and CSA (blue), and the full metasurface (red), all placed on a Si/SiO$_2$ substrate. (d) Average near-field enhancement $\eta = (E_t/E_{inc})^2$ over graphene surface. Insets: spatial distribution of η inside the gap for the two resonances. In (e) and (f) colors represent E_z calculated 5 nm below the metasurface/SiO$_2$ interface for EIT1 (e) and EIT2 (f). The electric current density for EIT1 (g) and EIT2 (h) are plotted inside the metal 5 nm above the interface.

of x-oriented monopole antennas[59,60] attached to the wire; and (iii) a C-shaped antenna (CSA) placed in their proximity. The plasmonic metasurface is assumed to be placed on a finite-thickness ($t = 1$ μm) SiO$_2$ substrate deposited on top of a Si wafer. The oxide layer is chosen to be thick enough to avoid any effect of the Si wafer on the near-field optical properties of the plasmonic metasurface. The finite reflection from the SiO$_2$/Si interface does, of course, contribute to the overall reflectivity, and is fully accounted for in our simulations presented below. This metasurface exhibits an optical response with two maxima in the transmission spectrum (or two deep reflectivity minima) due to Fano resonances, and therefore can be characterized as a plasmonic metasurfaces exhibiting double electromagnetically induced transparency (double-EIT). This effect is illustrated in Figure 2c, where we use a bottom-up approach of adding different constitutive parts of the unit cell to illustrate the nature of the two resonances as detailed below.

First, we note that a grid of plasmonic wires behaves as anisotropic "dilute plasma"[61] for the y-polarized incident light. Specifically, the structure strongly reflects the light with the wavelength λ which is longer than the characteristic effective plasmon wavelength λ_p^{eff}, which is a function of the interwire spacing P_x, wire width w, and the frequency-dependent dielectric permittivity ϵ_s (λ) of the underlying substrate. As expected, the reflectivity $R(\lambda)$ of the wire array shown as the black solid line in Figure 2c increases as a function of the wavelength and reaches 60% at $\lambda = 7.5$ μm. Next, a CSA supporting a dipolar antenna resonance at λ_d is added to the metasurface. The destructive interference between antiparallel currents in the wires and in the CSA for $\lambda > \lambda_d$ produces a pronounced dip in reflectivity at $\lambda_2 \approx 7.2$ μm, as shown by the blue line in Figure 2c. We refer to this dip as the EIT2. Although the dip at $\lambda = \lambda_2$ is not particularly narrow because of the strong coupling between the dipole-active mode of the CSA and the plasmonic wire, we demonstrate below that the half width at half-maximum (hwhm) $\sigma_{1/2}$ of the emerging reflectivity peak can be considerably narrowed by employing a second Fano resonance at the shorter wavelength.

Specifically, by adding the x-directed (horizontal) plasmonic monopole antennas to the wire grid, we introduce a second dark (monopole) mode whose resonant frequency corresponding to $\lambda_m \approx 6.2$ μm is primarily determined[59,60] by the monopoles' length l_m according to $\lambda_m \approx 4 l_m \sqrt{\epsilon_s}$. This emergent mode is referred to as the monopole mode because of the strong current flow between neighboring monopole antennas. Note that if the monopole antennas are equally spaced, that is $P_y = 2(L_y + w)$, then by symmetry the monopole mode is strictly dark (i.e., completely decoupled from the normally incident light and the concomitant uniform wire current) in the absence of the near-field coupling between the C-shaped and monopole antennas. The symmetry breaking produced by the introduction of the CSA antennas and by the nonequal spacing of the antennas causes the narrow-band monopole mode to couple to the broad-band wire grid currents, thus producing Fano interference. The destructive Fano interference between the wire current and the current flowing between the monopole antennas results in the short-wavelength reflectivity dip at $\lambda_1 \approx 6.2$ μm, which is referred to as the first EIT (EIT1) in the rest of the paper. The charge distribution and current profile for the EIT1 dip are shown in Figures 2e,g, respectively.

The addition of the monopole antennas also has an effect on the dipole mode and, by extension, on the EIT2 reflectance dip. By comparing the spectral positions of the EIT2 with (red line) and without (blue line) the monopole antennas, we conclude that the capacitive coupling between the CSAs and monopole antennas causes the spectral position of EIT2 to red-shift. The near-field coupling between C-shaped and monopole antennas produces a characteristic quadrupole-like charge distribution shown in Figure 2f, which is responsible for electric field enhancement between the antennas. This field enhancement plotted in Figure 2d can be exploited in graphene-functionalized metasurfaces as explained below. The near-field coupling between the two discrete (dipolar and monopolar) modes and the broad-band currents flowing in the plasmonic wire grid cause Fano interference. The result of this interference is a double-dip reflectivity spectrum shown in Figure 2c (red line). Qualitatively, the EIT2 reflectivity dip at $\lambda_2 \approx 7.6\ \mu$m is caused by the counter-flowing currents in the CSA and the wire grid plotted in Figure 2h. The resulting narrow reflectivity peak "sandwiched" between the EIT1,2 dips at λ_1 and λ_2 is the main consequence of the double-Fano resonance. It is exploited in this work in order to develop a graphene-based reflection modulator. The modulation is accomplished by electrically controlling the conductivity of graphene, which in turn detunes the reflectivity dips by a considerable fraction of the line width $\sigma_{1/2}$ of the reflectivity peak.

In order to achieve the largest possible spectral shift of Fano resonances by the addition of an SLG placed underneath the metasurface, it is important that it experiences the largest possible tangential component E_t of the electric field. Therefore, one of the functions of the metasurface is to produce a strong near-field enhancement $\eta = (E_t/E_{inc})^2$ of the incident electric field E_{inc} on the surface of graphene. This tangential field intensity enhancement, which determines the interaction energy between graphene and the metasurface, is plotted in Figure 2d as a function of the wavelength of the incident wave. The maxima of η correspond to the spectral positions of the Fano resonances.[9] Note that a much stronger tangential field enhancement is observed at $\lambda = \lambda_2$ compared to $\lambda = \lambda_1$, suggesting that the strongest coupling between the metasurface and SLG should be expected at the long-wavelength (second) Fano resonance.

We also note that the possibility of employing two discrete states strongly interfering with a continuum state has been discussed in the original paper by U. Fano,[64] and its application to multiband sensing applications was later suggested.[65] Here, we employ the double-Fano resonance for several purposes. First, we use the two Fano resonances in order to produce a narrow-band reflectivity maximum that can be utilized for dynamic modulation of reflectivity using SLG. Second, we experimentally demonstrate a dual-band SLG modulator that produces the highest degree of optical modulation at the frequencies corresponding to the two EIT resonances, λ_1 and λ_2. Third, we demonstrate that the degree of optical modulation (both in amplitude and phase), which is proportional to the frequency shifts $\Delta\omega_{1,2}$ due to the SLG's hybridization with the metasurface, depends on the tangential field distribution in graphene. For example, the charge distribution on the metasurface corresponding to the second (long-wavelength) Fano resonance supports much higher tangential field, resulting in $\Delta\omega_2 > \Delta\omega_1$. The consequence of this hierarchy of Fano resonances is that the modulation depth around $\lambda = \lambda_2$ is larger than that around $\lambda = \lambda_1$.

Extending the earlier developed theory[50,66] of Fano-resonant metasurfaces which demonstrated that the complex-valued reflectivity coefficient $r(\omega)$ from a metasurface supporting a single Fano resonance can be described by a two-pole (double-Lorentzian) function, we approximate the reflectivity from a double-Fano resonant metasurface using the following triple-Lorentzian function:

$$r(\omega) = \frac{A_0}{i\omega - 1/\tau_0} + \frac{A_m}{i(\omega - \omega_m) - 1/\tau_m} + \frac{A_d}{i(\omega - \omega_d) - 1/\tau_d} \qquad (1)$$

where $\omega_{m(d)}$ and $\tau_{m(d)}$ are the spectral positions and lifetimes of the monopole (dipole) resonances of the "bare" (i.e., without graphene) metasurface. The first term in eq 1 describes the broadband reflectivity by the plasmonic wires, the second term describes the resonant reflectivity by the monopole resonance, and the third term describes the resonant reflectivity by the CSA resonance. The complex amplitudes A_0, A_m, A_d (where $A_0 \gg A_m$, A_d, see the details in the Supporting Information) of the corresponding modes are proportional to their far-field coupling strength.[50,66] Note that, in general, the resonance frequencies do not coincide with the spectral positions of the reflectivity dips: $\omega_{1(2)} \neq \omega_{m(d)}$. The corresponding quality factors of the two resonances defined as $Q_{m(d)} = \omega_{m(d)}\tau_{m(d)}$ will be computed below from the experimental data by fitting the reflectivity spectrum $R(\lambda \equiv 2\pi c/\omega)$ to the $|r(\omega)|^2$ function given by eq 1.

Integration of the Metasurface with Graphene. The multipole expansion of the reflectivity coefficient remains valid after loading the metasurface with SLG. The addition of an SLG perturbs the resonant frequencies of the bare (graphene-free) metasurface according to $\tilde{\omega}_{m(d)} = \omega_{m(d)} - i/\tau_{m(d)} + \Delta\tilde{\omega}_{m(d)}$, where the graphene-induced complex-valued frequency shift $\Delta\tilde{\omega}_{m(d)}$ is calculated[42] according to

$$\Delta\tilde{\omega}_{m(d)} = -i\sigma_{SLG}\int_S |E_t|^2 dS/W_0^{m(d)} \qquad (2)$$

where $\sigma_{SLG}(\omega) \equiv \sigma_{re} + i\sigma_{im}$ is the complex-valued surface conductivity of the SLG represented as the sum of it resistive and reactive parts, $W_0^{m(d)}$ is the stored energy of the given (monopole or dipole) mode, and the integration is performed over graphene's surface S.

It follows from eq 2 that the addition of graphene has two effects: (a) spectral blue-shift of the resonant frequencies $\omega_{m(d)}$ equal to $\Delta\omega_{m(d)} = Re[\Delta\tilde{\omega}_{m(d)}] \propto \sigma_{im}$, and (b) additional spectral broadening of the mode, that is, the increase of the quantity $1/\tau_{m(d)}$, which is equal to $\Delta(1/\tau_{m(d)}) = -\mathcal{I}m[\Delta\tilde{\omega}_{m(d)}] \propto \sigma_{re}$. According to eq 2, these frequency/lifetime changes are proportional to the square of the tangential electric field of each mode on graphene, thus suggesting that the dipole resonance should experience larger perturbation that the monopole resonance according to Figure 2d. Spectral tuning of the optical response of the graphene-functionalized metasurface is accomplished by injecting free charge carriers into graphene. Its conductivity, $\sigma_{SLG}(\omega)$, depends on the areal concentration n of the free carriers (electrons or holes) which is parametrized by the Fermi energy $E_F = \hbar V_F(\pi n)^{1/2}$, where V_F is the Fermi velocity. For the typical $V_F = 1.1 \times 10^8$ (cm/s), the Fermi energy is related to n through a simple relationship $E_F = (n\,[\mathrm{cm}^{-2}])^{1/2}/(7.8 \times 10^6)$ eV. Under the random phase approximation (RPA),[79] graphene's conductivity can be broken up into two contributions according to $\sigma_{SLG}(\omega) = \sigma_{inter}(\omega) + (\omega)_{intra}(\omega)$, where

$$\sigma_{inter}(\omega) = \frac{e^2}{4\hbar}\left[\frac{1}{2} + \frac{1}{\pi}\tan^{-1}\left(\frac{\hbar\omega - 2E_F}{2k_BT}\right) - \frac{i}{2\pi}\ln\frac{(\hbar\omega + 2E_F)^2}{(\hbar\omega - 2E_F)^2 + (2k_BT)^2}\right]$$
$$\sigma_{intra}(\omega) = \frac{e^2}{4\hbar}\frac{8ik_BT}{\pi\hbar(\omega + i\tau^{-1})}\ln\left[2\cosh\left(\frac{E_F}{2k_BT}\right)\right] \qquad (3)$$

are due to the interband and intraband transitions, respectively. In eq 3, k_B is the Boltzmann constant, T is the temperature, ω is the frequency of IR light, and τ is the free carrier scattering rate.

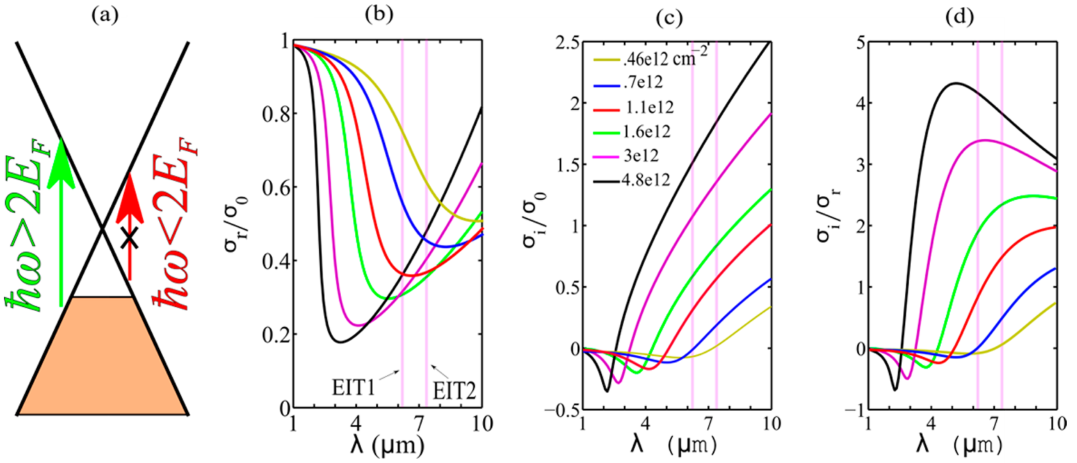

Figure 3. Optical properties of graphene. (a) Pauli blocking: interband losses are suppressed for $\hbar\omega < 2E_F$. (b) Real and (c) imaginary parts of graphene's optical sheet conductivity $\sigma_{SLG}(\omega)$ calculated from eq 3 for different values of graphene doping. (d) Ratio of inductive to resistive conductivities for different free carrier densities in graphene color-coded according to the inset in (c). Carrier scattering time: τ = 18 fs.

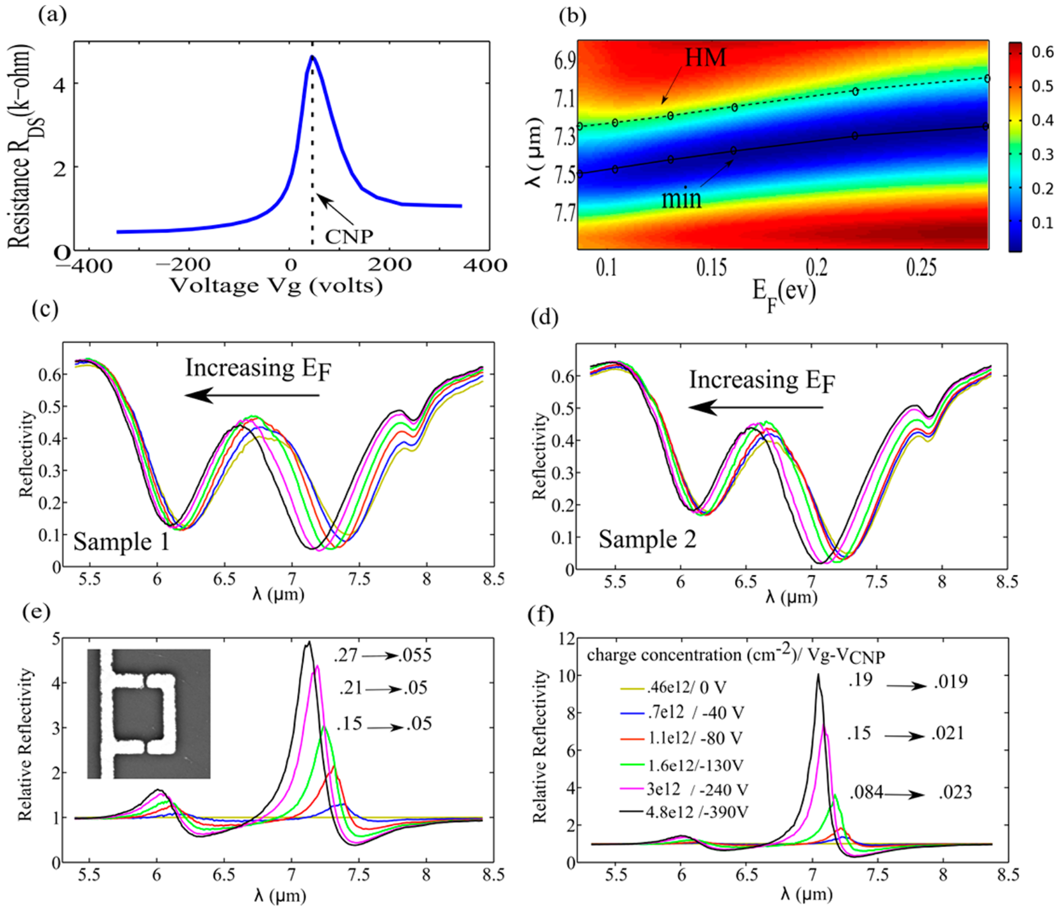

Figure 4. Experimentally measured reflectivity modulation from a plasmonic metasurface (see inset) integrated with back-gated graphene. (a) Measured drain-source dc electric resistance of the SLG vs gate voltage V_g (see Figure 1b). Charge neutrality point: $V_{CNP} \approx +45V$. (b) Color-coded reflectivity from the sample 1 in the vicinity of the dipole resonance. The minimum (min) and the half-maximum (HM) of the reflectivity spectrum are shown for different Fermi energies E_F. (c, d) Reflectivity spectra for the samples 1 (c) and 2 (d). The spectra are color-coded according to the values of $n(\Delta V)$ tabulated in (f). Inset in (c): SEM image of the unit cell of the metasurface fabricated on top of the CVD graphene. (e, f) Relative reflectivities (extinction ratios) RR(n,λ) corresponding to the spectra in (c, d). Insets: baseline reflectivity $R_{on}(\lambda)$ at $\Delta V = 0$ and the extinguished reflectivity $R_{off}(n_h,\lambda)$ for the 3 highest holes' concentrations n_h corresponding to the maximum of RR(n,λ).

The real and imaginary parts of the graphene conductivity $\sigma_{SLG}(\omega)$, measured in the units of universal optical conductivity $\sigma_0 = e^2/4\hbar$, are plotted in Figures 3b,c, respectively, as functions of the wavelength $\lambda = 2\pi c/\omega$. The estimated (see below for details) scattering time τ = 18 fs (corresponding to the carrier scattering rate τ^{-1} = 293 cm^{-1}) was assumed. A dip of σ_{re} is observed at intermediate wavelengths (e.g., $\lambda > 5\ \mu$m) due to the Pauli blocking of loss-inducing interband transitions as illustrated in Figure 3a. The plasmonic response of graphene can be quantified by the ratio $(\sigma_{im}/\sigma_{re})$,[50] which was recently measured by launching graphene plasmons using near-field scanning optical microscopy.[75] As Figure 3d shows, the higher the charge concentration, the larger this ratio becomes, making graphene increasingly plasmonic.

The carrier collisional time τ can be estimated using two independent approaches. The first approach[51,73] utilizes experimentally measured dc electrical conductivity σ_{DC} of the graphene sheet for calculating τ. We estimate[74] that $\tau^{(DC)} = \sigma_{DC}\hbar^2/2e^2E_F \approx 14$ fs (see Methods). One drawback of this approach is that σ_{DC} is averaged over a large area of graphene that lies outside of the regions of optical energy concentration. Therefore, the measured conductivity σ_{DC} can be effectively reduced due to, for example, carrier scattering at grain boundaries[75] that may be present outside of the relevant gap between the C-shaped and monopole antennas where the optical energy is concentrated as shown in Figure 2d. Therefore, the relevant scattering time can be easily underestimated by the value of $\tau^{(DC)}$. To improve the accuracy of estimating τ, we have developed a new experimental technique (described later in this work), which is based on comparing the quality factors and spectral positions of the Fano resonances of graphene-loaded metasurfaces with their unloaded counterparts. It was found that $\tau = 18fs$ (corresponding to the collisional frequency $\tau^{-1} = 293$ cm^{-1}), which is the value used in Figure 3.

EXPERIMENTAL RESULTS

Reflectivity Modulation/Switching Using Gated Graphene. Two metasurfaces with physical dimensions given in the caption of Figure 2 were fabricated on top of an SLG grown using chemical vapor deposition (CVD) and transferred onto an oxidized Si wafer (see Methods). The carrier density n in graphene was controlled by an applied electrostatic potential difference between the SLG and the Si backgate according to $n \cong (n_0^2 + (C_g\Delta V/e)^2)^{1/2}$, where n_0 is the residual carrier density[73] at the charge neutrality point (CNP), and $\Delta V = V_g - V_{CNP}$ is the potential deviation from the CNP voltage V_{CNP}. The experimental value of the $V_{CNP} \approx +45V$ corresponding to the maximum of graphene's resistance was experimentally determined from the electric measurements of graphene resistance[67] plotted in Figure 4a. The gate capacitance per unit area $C_g = \varepsilon/d$, where d and ε are the thickness and electrostatic permittivity of the SiO$_2$ spacer, was estimated to be $C_g \approx 2nF$ cm^{-2} for our sample. The residual charges at the CNP point were estimated to be around $n_0 = 4.6e\ 11$ cm^{-2} using the standard technique,[74] as detailed in Methods. All experiments were carried out in the hole-injection regime of $\Delta V < 0$.

The reflectivity spectra $R(n,\lambda)$ from graphene-integrated Fano-resonant metasurfaces are plotted in Figure 4c,d for samples 1 ($G = 70$ nm) and 2 ($G = 100$ nm), respectively. The spectra are color-coded according to the values of carrier (hole) concentrations $n \equiv n_h$ in the SLG described in Figure 4f inset. The color-coded spectra for the sample 1 in the vicinity of the dipole resonance (close to the EIT2 reflectivity dip) are replotted in Figure 4b to illustrate that the spectra are shifted by more than hwhm of the reflectivity peak by changing the free carrier areal density in graphene from $n = n_0$ to $n_{max} = 4.8 \times 10^{12}$ cm^{-2}. This remarkably strong effect of graphene on the reflectivity is caused by two properties of the graphene-loaded metasurface: (i) narrow spectral width of the reflectivity peak and (ii) strong concentration of the tangential electric field. While the most dramatic modulation of the reflected intensity is observed near the EIT2 dip (around $\lambda_2^{mod} \approx 7\ \mu$m), a weaker (but comparable with the present state-of-art results[75]) modulation is also observed near the EIT1 dip (around $\lambda_1^{mod} \approx 6\ \mu$m).

To quantify the efficacy of the resulting graphene/metasurface modulator, we define the wavelength-dependent modulation depth (MD) as[56,68,69]

$$MD(n, \lambda) = \left|\frac{R_{on}(\lambda) - R_{off}(n, \lambda)}{R_{on}(\lambda)}\right| \times 100\% = \left|1 - \frac{1}{\mathrm{RR}(n, \lambda)}\right| \times 100\% \quad (4)$$

Here $\mathrm{RR}(n, \lambda) = R_{on}(\lambda)/R_{off}(n, \lambda)$ is the extinction efficiency that represents the ratio between the baseline reflectivity $R_{on}(\lambda) \equiv R(n = n_0,\lambda)$ measured in the absence of free carriers in the SLG and the extinguished reflectivity $R_{off}(n,\lambda) \equiv R(n,\lambda)$ measured for the gate voltage corresponding to the finite gate-induced carrier concentration $n = n_h$. Relative reflectivities $\mathrm{RR}(n,\lambda)$ for the samples 1 and 2 are plotted in Figure 4e and f, respectively. The higher is the relative reflectivity, the better is the modulator. Ideally, one would prefer that both the baseline reflectivity $R_{on}(\lambda)$ and the relative reflectivity $\mathrm{RR}(n_h^{max},\lambda)$ corresponding to the largest applied voltage be large numbers. For example, a modulator with a low value of the baseline reflectivity would be inefficient regardless of its relative reflectivity. As our experimental results presented in Figure 4c,d indicate, these two requirements can indeed be satisfied by a Fano-resonant metasurface integrated with back-gated SLG.

Specifically, large values of the peak RR, defined as $\mathrm{RR}_{peak} = \max \mathrm{RR}(n_h^{max},\lambda)$, are experimentally measured around λ_2^{mod} for both samples. For sample 1, $\mathrm{RR}_{peak}^{(1)} \approx 5$ leading to $\mathrm{MD}_{peak}^{(1)} \approx 80\%$ (corresponding to extinguishing the baseline reflectivity from 27% down to 5.5%) is demonstrated, while an even higher $\mathrm{RR}_{peak}^{(2)} \approx 10$ leading to $\mathrm{MD}_{peak}^{(2)} \approx 90\%$ (corresponding to extinguishing the baseline $R_{on} = 19\%$ reflectivity down to $R_{off} = 1.9\%$) is achieved for sample 2. Better performance of the modulator based on sample 2 can be explained by considerably lower value of R_{off} which, in turn, is caused by its higher quality factor. We note that these modulators are relatively narrow band because of the resonant nature of the metasurface. For example, the 3 dB bandwidth of the modulation depth was measured to be $\Delta\lambda^{(1)} = 245$ nm and $\Delta\lambda^{(2)} = 140$ nm (corresponding to 3.5% and 2% of the resonance wavelength) for samples 1 and 2, respectively. We also observe that the RR is much smaller for the shorter-wavelength monopole mode at $\lambda_1^{mod} = 6\ \mu$m. This is a direct consequence of the weaker tangential field enhancement η at the monopole resonance as observed from the theoretical calculation shown in Figure 2d.

Note that the small feature at $\lambda \approx 7.9\ \mu$m is due to the occurrence of epsilon near zero (ENZ) effect that stems from the longitudinal phonon polariton resonance of SiO$_2$, where $\varepsilon_r^{SiO_2} = 0$.[63,70] This resonance is excited by the electric field component of the incident light (E_z), which is normal to the substrate. Therefore, it is predicted to appear for finite incidence angle and P-polarized incident field. These are indeed the experimental conditions encountered in our experiment because of the inherent properties of the focusing optics of the infrared microscope.

The existence of an optical phonon at $\lambda_{SiO_2} \approx 9\ \mu$m[62,63] and the strongly dispersive character of the substrate's dielectric permittivity $\epsilon_{\mathrm{SiO_2}}(\omega) \equiv \epsilon_r + i\epsilon_{im}$ affect the quality factor of the dipole resonance. Specifically, the resonant behavior of $\epsilon_r(\omega)$ causes the quality factor of the dipole mode to increase in comparison with the case of an idealized (nondispersive) substrate that is typical for visible/near-IR frequency range. As a result, the Q-factors of the dipole and monopole resonances are comparable despite the fact that the dipole resonance is brighter than the monopole resonance. Additional information about the substrate effect is provided in the Supporting Information.

As mentioned earlier, an ideal modulator needs to be both efficient (high baseline reflectivity, i.e., moderate insertion loss) and possess a high modulation depth. Achieving high MD by itself is not particularly challenging: as long as the reflectivity drops to near-zero value (as it is indeed the case according to Figure 4c,d of the metasurface under this study), even the slightest spectral detuning of the Fano resonance will result in a high MD. Simultaneously satisfying the efficiency requirement is more challenging because it requires that the spectral detuning $\Delta\lambda_{\mathrm{m(d)}}$due to graphene be comparable to $\sigma_{1/2}$. Therefore, in order to understand how the SLG shifts the frequencies and quality factors of the two Fano resonances, we have fitted the experimentally measured reflectivity spectra $|r(\omega)|^2$ for the sample 1 to the triple Lorentzian formula given by eq 1. The details of the fitting procedure and the values of the fitting parameters can be found in the Supporting Information. The results of the fitting procedure for the three selected concentrations of charge carriers are shown in Figure 5a. The ENZ feature has been excluded from the fitting window.

The resonant wavelengths $\lambda_{\mathrm{m(d)}}$ and quality factors $Q_{\mathrm{m(d)}}$ for the two resonances are plotted in Figure 5 for increasing doping levels n_{h}. According to Figure 5b,e, the resonant wavelengths first slightly increase for small values of n_{h} because $\sigma_i(\lambda_{\mathrm{m(d)}}) < 0$ due to the interband term,[36,50] as shown in Figure 3c. This spectral detuning is very small for carrier concentrations corresponding to interband transitions-dominated regime which is defined by $2E_{\mathrm{F}}(n) < \hbar\omega_{\mathrm{d(m)}}$ and bounded by the vertical dashed lines in Figure 5. At the same time, as the Pauli blocking starts taking place for $2E_{\mathrm{F}}(n) > \hbar\omega_{\mathrm{d(m)}}$, the quality factor of both resonances experiences a rapid increase shown in Figures 5c,f by the red circles. The rise in the Q-factors (QFs) correlates with the decrease of the real (dissipative) part of graphene's surface conductivity σ_{r}, shown by the blue circles in Figure 5c,f. Overall, the transition to Pauli blocking regime for high values of carrier density causes considerable change of the QFs for both modes: the Q's of the monopole and dipole mode change in the $14.3 < Q_{\mathrm{m}} < 16.4$ range (15%) and in the $15.0 < Q_{\mathrm{d}} < 18.2$ range (21%), respectively. Note that the maximum of QF approximately coincides with the minimum of σ_{r} for both modes.

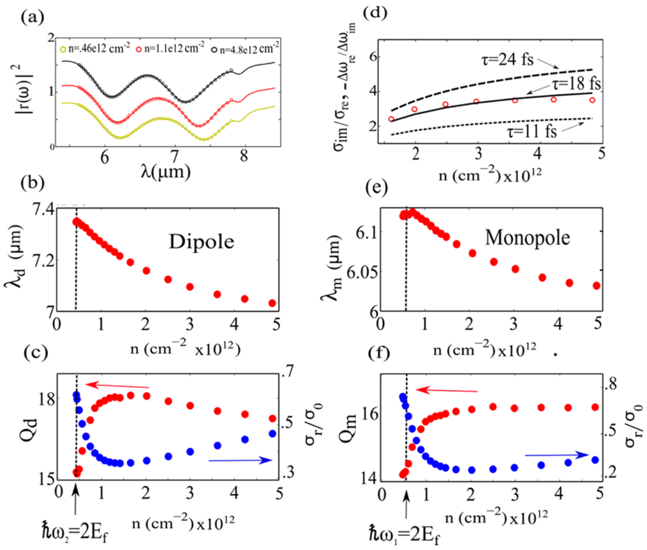

Figure 5. (a) Measured reflectivity spectrum (solid lines) for sample 1, fitted to the tri-Lorentzian spectrum given by eq 1 (circles) for three selected holes' concentrations. (b, c) Extracted resonant wavelengths $\lambda_{\mathrm{d}}(n)$ and the quality factor $Q_{\mathrm{d}}(n)$ of the dipole mode. (d) Extraction of the holes' scattering time τ in the Drude-dominated regime. Lines: $\sigma_{im}^n/\sigma_{re}^n$ calculated for three values of free carrier scattering time τ, circles: ratio of graphene-induced frequency shifts: $Re[\Delta\tilde{\omega}^n_{\mathrm{m(d)}}]/Tm[\Delta\tilde{\omega}^n_{\mathrm{m(d)}}]$ of the resonances for a range of carrier concentrations. (e, f) same as (b, c), but for the $\lambda_{\mathrm{m}}(n)$ and $Q_{\mathrm{m}}(n)$ of the monopole mode. Vertical dashed lines: carrier concentration n corresponding to $2E_{\mathrm{F}}(n) = \hbar\omega_{\mathrm{d,m}}(n)$. Blue circles in (c) and (f): σ_{re} in units of the universal conductance $\sigma_0 = e^2/4\hbar$ calculated at corresponding resonant frequencies $\omega_{\mathrm{d,m}}(n_{\mathrm{h}})$.

Spectral blue-shifting of both resonances can be clearly observed in Figure 5b,e as the carrier density increases. This experimentally observed behavior is consistent with eq 2. For example, for the dipole mode the spectral shift is $|\Delta\lambda_{\mathrm{d}}| \approx 0.33\ \mu$m ($\Delta\omega_{\mathrm{d}} \approx 62^{-1}$) or about $|\Delta\lambda_{\mathrm{d}}|/\lambda_{\mathrm{d}} \approx 4.6\%$. Assuming that $Q_{\mathrm{d}} \approx 18$, we conclude that the $|\Delta\lambda_{\mathrm{d}}|/\lambda_{\mathrm{d}} > 1/2Q_{\mathrm{d}}$ condition, which is necessary for an efficient and deep modulator, is satisfied for the dipole resonance of the integrated graphene/metasurface structure. On the other hand, the corresponding spectral shift numbers for the monopole resonance (EIT1) are more modest: $|\Delta\lambda_{\mathrm{m}}| \approx 0.09\ \mu$m ($\Delta\omega_{\mathrm{m}} \approx 23$ cm^{-1}) or about $|\Delta\lambda_{\mathrm{m}}|/\lambda_{\mathrm{m}} \approx 1.4\%$. The spectral shift of the monopole mode is considerably smaller than that of the dipole mode, which is mainly due to its weaker interaction with graphene (smaller tangential field enhancement η), as shown in Figure 2d. We also note that the spectral shifting of the plasmonic metasurface resonances can be entirely contributed to carrier injection into SLG and not to the effect of electric gating on carrier density in Si because of the very low doping ($n_{\mathrm{Si}} \approx 10^{15}$ cm^{-3}) of the substrate, as well the large separation ($t = 1\ \mu$m) of the substrate from the metasurface.

Metasurface-Based Measurement of Carrier Scattering Rate. Below we demonstrate that spectral shifts and line width changes produced from loading plasmonic metasurfaces with gated graphene can be used for precise determination of graphene's optical properties. Specifically, the free carrier scattering rate τ can be determined using a simple procedure. In the presence of the graphene monolayer, the denominators $(\omega_{\mathrm{m,d}} - i/\tau_{\mathrm{m,d}})$ in eq 1 need to be replaced by density-dependent complex-valued resonant frequencies $\tilde{\omega}^n_{\mathrm{m(d)}}$, where

$$\tilde{\omega}^n_{\mathrm{m(d)}} = \omega_{\mathrm{m(d)}} - i/\tau_{\mathrm{m(d)}} + \Delta\tilde{\omega}^n_{\mathrm{m(d)}} \tag{5}$$

These frequencies are obtained by numerically fitting the absolute square of eq 1 to the reflectivity data that was experimentally measured for a broad range of carrier densities $n_0 < n < 4.8e\ 12$ cm^{-2}. The corresponding resonant wavelengths and quality factors defined, respectively, as $\lambda_{\mathrm{m(d)}} \equiv 2\pi c/Re(\tilde{\omega}_{\mathrm{m(d)}})$ and $Q_{\mathrm{m(d)}} \equiv Re(\tilde{\omega}_{\mathrm{m(d)}})/\mathcal{I}m(\tilde{\omega}_{\mathrm{m(d)}})$ are plotted in Figure 5 as a function of carrier density n. The actual values of the frequencies $Re(\tilde{\omega}_{m(d)})$ (in units of cm^{-1}) and lifetimes $\tau_{\mathrm{m(d)}} \equiv 1/\mathcal{I}m(\tilde{\omega}_{\mathrm{m(d)}})$ (in units of femtoseconds) are listed in Table S2 of the SOI.

According to eq 2, graphene-induced complex frequency shifts $\Delta\tilde{\omega}^n_{\mathrm{m(d)}}$ satisfy[50] the following equation:

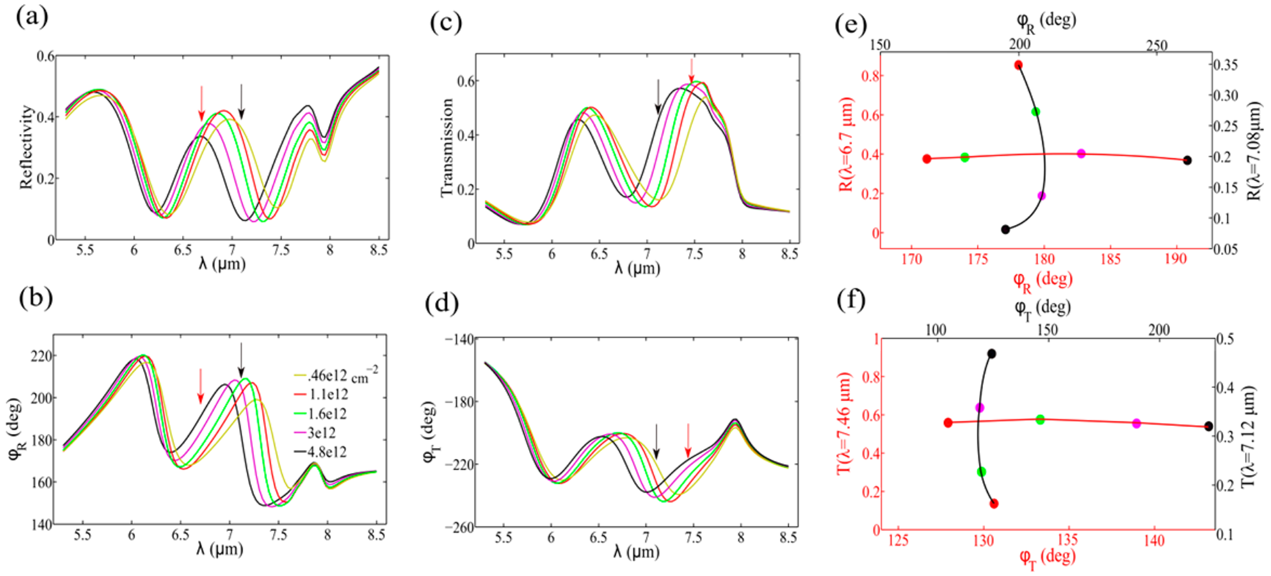

Figure 6. Numerical simulations of (a) intensities and (b) phases of the reflected light, and (c) intensities and (d) phases of the transmitted light for Sample 1 ($G = 70$ nm) at different graphene doping levels. The arrows indicate the spectral positions with constant scattering intensities (red arrows) and phase (black arrows). (e) Differently replotted intensities/phase of the reflected light for $\lambda_R^{PM} = 6.7\ \mu$m (red curves/axes) and $\lambda_R^{AM} = 7.08\ \mu$m (black curves/axes) for four different doping values. (f) Same as (e) but for transmitted light at $\lambda_T^{PM} = 7.46\ \mu$m (red curves/axes) and $\lambda_T^{AM} = 7.12\ \mu$m (black curves/axes). Graphene doping levels in (e) and (f) are color-coded according to the legend in (b).

$$\frac{Re[\Delta\tilde{\omega}^{n}_{\mathrm{m(d)}}]}{Tm[\Delta\tilde{\omega}^{n}_{\mathrm{m(d)}}]} = -\frac{\sigma_{im}(\omega_{\mathrm{m(d)}},\, n)}{\sigma_{re}(\omega_{\mathrm{m(d)}},\, n)} \qquad (6)$$

where graphene's conductivity $\sigma_{\mathrm{SLG}}(\omega_{\mathrm{m(d)}},n)$ is calculated at the resonant frequencies $\omega_{\mathrm{m(d)}}$ of the bare (graphene-free) metasurface. Equation 6 expresses a novel opportunity for characterizing optical properties of graphene (rhs of the equation) using experimentally measured frequency shifts of metasurface resonances (lhs of the equation). This approach is particularly valuable in the mid-IR portion of the spectrum where traditional transmission/absorption spectroscopy of graphene[76] is challenging because σ_{re} of the SLG is much smaller than the universal conductance $\sigma_0 = e^2/4\hbar$, as shown in Figure 3b,c. Under such circumstances, very small (<1%) changes in transmission through graphene must be accurately measured in order to extract graphene's optical parameters such as, for example, its carrier scattering rate τ.

We have used a best-fit procedure using two time scale (τ and the dipole mode lifetime τ_{d} for a bare metasurface) as fitting parameters to extract the scattering rate for sample 1 (see Methods for details). The complex-valued frequency and lifetime shifts $\Delta\tilde{\omega}^{\mathrm{n}}_{\mathrm{d}}$ induced by graphene and, therefore, the left-hand side (lhs) of eq 6, can be calculated from eq 5 assuming that ω_{d} and τ_{d} are given. In fact, the bare metasurface's resonance frequency ω_{d} was extracted from a simulation, while τ_{d} is a priori unknown. Likewise, the right-hand side (rhs) of eq 6 is calculated using eq 3, where τ is a priori unknown. Thus, both the lhs and the rhs of eq 6 contain an unknown parameter: τ_{d} and τ, respectively. The best-fit values of τ_{d} and τ were calculated by minimizing the difference between the lhs and rhs over a wide range of hole densities $1.5e\ 12\ \mathrm{cm}^{-2} < n < 4.8e\ 12\ \mathrm{cm}^{-2}$. The carrier density range was chosen to ensure that Drude conductivity contribution $\sigma_{\mathrm{intra}}(\omega)$ dominates over the interband conductivity contribution $\sigma_{\mathrm{intra}}(\omega)$, and to ensure that gating-induced free carrier density is much larger than the residual density n_0 at the CNP point. The dipole resonance was chosen over the monopole resonance because according to Figure 2c,d the effect of graphene on the former is much larger than on the latter.

The lhs of eq 6 given by $E(n;\ \tau_{\mathrm{d}}) \equiv -Re[\Delta\tilde{\omega}^{n}_{\mathrm{d}}]/Tm[\Delta\tilde{\omega}^{n}_{\mathrm{d}}]$ is plotted in Figure 5d using the best-fit result for τ_{d} for seven values of n (open circles) alongside with the rhs of eq 6 given by $T(n;\ \tau) \equiv \sigma_{im}(\omega_{\mathrm{d}},n)/\sigma_{re}(\omega_{\mathrm{d}},n)$ calculated for three values of hole scattering time: $\tau_1 = 11$ fs, $\tau_2 = 18$ fs, and $\tau_3 = 24$ fs (where $\tau_{\mathrm{d}} = \tau_2$ corresponds to the best-fit value). According to eq 6, these two quantities must be equal under the assumption that τ does not depend on the density of free carriers. It follows from Figure 5d that this equality is rather accurately satisfied only for the fitted value of τ_2. Therefore, our experimental results impose very restrictive limits on the value of τ. We note that $\tau^{(\mathrm{DC})} \approx 14$ fs, obtained using dc conductivity measurements, is indeed an underestimate of the actual scattering time. As argued above, this may be related to the presence of grain boundaries outside of the optical field concentration areas of the metasurface.

Comparisons with Numerical Simulations and Prospects for Independent Amplitude/Phase Modulation. Numerical simulations were carried out in order to verify the experimental results presented in Figures 4 and 5. In addition, these numerical simulations enable us to make predictions about some of the physical quantities that were not experimentally measured in this work, such as the amplitude and phase of the transmitted waves. The dielectric permittivities of Au and $\mathrm{SiO_2}$ were taken from the Palik handbook of optical constants[71] in all simulations. Figure 6a,b show the simulated reflection amplitudes $R(\lambda) \equiv |r(\lambda)|^2$ and phases $\varphi_R(\lambda)$ of the reflected light for different carrier concentrations, and Figure 6a is in excellent quantitative agreement with the experimentally measured spectra shown in Figure 4c. For completeness, we also present in Figures 6c,d the numerically simulated transmittances $T(\lambda)$ and phases $\varphi_T(\lambda)$ of the transmitted light although no experimental measurements of the transmission were performed at this time. All simulations are performed for sample 1 with the gap size of 70 nm. The incidence light is chosen to be P-polarized with the angle of incidence $\theta_i = 25°$ for consistency with our experimental setup that utilizes a high-NA microscope.

Below we use the results of the numerical simulations to demonstrate the promise of graphene-functionalized Fano-resonant metasurfaces for developing rapidly tunable amplitude and phase modulators (AM and PM) that can potentially operate with nanosecond-scale modulation speeds. We demonstrate that nearly pure phase modulation can be achieved at certain wavelengths (shown by red arrows in Figures 6a,b for reflected light and Figure 6c,d for transmitted light). For other wavelengths (shown by black arrows in Figure 6a,b for reflected light and Figure 6c,d for transmitted light) nearly pure amplitude modulation occurs as the carrier concentration changes. Specifically, in Figure 6e we plot the reflection data for four values of carrier density varying between $n = 1.6e12$ and $n = 4.8e$ 12 cm^{-2} (color-coded circle symbols) for two specific wavelengths ($\lambda_R^{\text{PM}} = 6.7$ μm and $\lambda_R^{\text{AM}} = 7.08$ μm) in the (φ_R, R) phase plane. We observe that, for a fixed wavelength $\lambda = \lambda_R^{\text{PM}}$, the reflection phase $\varphi_R(\lambda_R^{\text{PM}})$ varies by almost $\Delta\varphi_R \approx 20°$ degrees as the function of n, while the reflection amplitude $R(\lambda_R^{\text{PM}})$ changes by only 3% for the same variation of carrier density. The implication of this result is that one can develop a narrow-band PM which only affects the phase but not the amplitude of the reflected light. For example, if different elements of the metasurface can be independently controlled, one can envision an active beam steering reflect-array that is based on SLG-functionalized metasurface.

Similarly, a narrow-band AM that affects the amplitude but not the phase of the reflected light can be implemented at $\lambda = \lambda_R^{\text{AM}}$: according to Figure 6e, the reflectance $R(\lambda_R^{\text{AM}})$ varies by factor 5 (from $R = 0.07$ to $R = 0.35$), whereas the phase $\phi_R(\lambda_R^{\text{AM}})$ changes by only $\Delta\varphi_R \approx 16°$ for the same variation of graphene's carrier density. Likewise, in Figure 6f we plot the transmission for two selected wavelengths ($\lambda_T^{\text{PM}} = 7.46$ μm and $\lambda_T^{\text{AM}} = 7.12$ μm) in the (φ_T, T) phase plane. Phase modulation without amplitude change can be achieved in transmission at $\lambda = \lambda_T^{\text{PM}}$: the transmission phase $\varphi_T(\lambda_T^{\text{PM}})$ varies by almost $\Delta\varphi_T \approx 16°$ as the function of n, while the transmission amplitude $T(\lambda_T^{\text{PM}})$ changes by only 3% for the same variation of carrier density. Similarly, amplitude modulation without phase change can be achieved in transmission at $\lambda = \lambda_T^{\text{AM}}$: the transmission amplitude $T(\lambda_T^{\text{AM}})$ changes by a factor 3 (from $T = 15\%$ to 45%), while the transmission phase $\varphi_T(\lambda_T^{\text{AM}})$ changes by only $\Delta\varphi_T \approx 7°$. By controlling both the amplitude and the phase of the individual segments of a metasurface, one can now envision actively controlled planar structures capable of forming infrared holograms[72] and infrared scene projectors of almost unlimited complexity operating in either transmission or reflection.

■ CONCLUSIONS

We have experimentally demonstrated electrical control of the reflectivity of mid-infrared light using back-gated single layer graphene. An order of magnitude modulation of the reflected light was accomplished by designing a novel type of a metasurface supporting double Fano resonances and integrating it with an under-layer of graphene. The unique aspect of such modulator is its high baseline reflectivity and large reflectivity extinction coefficient (modulation depth). A new metasurface-based approach to extracting the free carrier scattering rate in graphene was also demonstrated. Numerical simulations indicate that independent amplitude and phase modulation are possible in reflection and transmission. This work paves the way to future development of ultrafast optoelectronic devices such as dynamically reconfigurable holograms, single-detector imagers, dynamical beam-steering devices, and reconfigurable biosensors. Future work may be aimed at reducing the required gating voltage, which could be accomplished by using high-k dielectrics as insulating spacers between graphene and the conducting substrate.

■ METHODS

Sample Fabrication. The process of sample fabrication followed the steps below. First, the SLG was grown on polycrystalline Cu foil using a CVD technique[77] and subsequently transferred from the Cu foil onto 1 μm thick insulating (SiO_2) layer that was grown on a lightly doped silicon substrate[78] using wet thermal oxidation. Second, two 100 μm × 100 μm metasurface samples with unit cell dimensions given in Figure 2 and two different gaps ($G = 70$ nm for sample 1 and $G = 100$ nm for sample 2) between the CSAs and monopole antennas were fabricated on top of the SLG using electron beam lithography (EBL). The thickness of the metasurface was 30 nm (5 nm of Cr and 25 nm of Au). An SEM image of a segment of the sample 1 is shown in Figure 2b, where the inset zooms in on a single unit cell of the metasurface on SLG. Finally, source and drain contacts (10 nm Cr + 100 nm Au) were deposited on top of graphene on both sides of the samples using another EBL step. Back-gating voltage applied across the SiO_2 insulating layer between the Si substrate and the drain electrode was used to modulate graphene's carrier density, as shown in Figure 1b.

Graphene Characterization and Gating. SLG's characterization was carried out using current−voltage ($I-V$) measurements. The charge neutrality point (CNP) $V_g = V_{\text{CNP}} = 45V$ corresponding to $E_F = 0$ is identified by measuring the drain-source electric resistance $R_{\text{DS}}(V_g)$, as shown in Figure 4a. The hole mobility μ_h of graphene at room temperature was calculated from the measured electrical conductivity according to $\mu_h = \sigma(n_h)/n_h e \approx 3800$ $\text{cm}^2/(\text{V s})$, where $\sigma(n_h)$ is the electrical conductivity of graphene at the hole concentration n_h. We used $n_h = 4.8e$ 12 cm^{-2} for this calculation. The carrier collisional time can also be calculated[73] from the measured dc electrical conductivity to be $\tau = ((\sigma\hbar^2)/(2e^2E_F)) \approx 14$ fs, which is consistent with the value of τ derived using the optical conductivity of graphene, as explained in the Supporting Information. The residual carrier density at the CNP point was calculated as $n_0 = ((\sigma_{\min}n_{\text{imp}}h)/(20e^2)) = 4.6e$ 11 cm^{-2}, where $\sigma_{\min}$ is the minimum dc conductivity, and $n_{\text{imp}} \approx 1.3e$ 12 cm^{-2} is the concentration of charged impurities in a SiO_2 substrate, which is estimated from graphene's mobility.[74] The slight p-doping of the SLG by the SiO_2 substrate is inferred from $V_{\text{CNP}} > 0$. Due to the breakdown voltage of silicon dioxide at 0.5 GV/m, we vary the back gate voltage in the -345 $V < V_g < 45$ V range using "Heathkit 500 V PS-3" power supply. The holes' areal concentration (given by $n_h = C_g\Delta V/e$) can reach the maximum values of $n_h^{\max} \approx 4.8e$ 12 cm^{-2} for the peak gate voltage.

Optical Measurement. Optical characterization of back-gated metasurfaces integrated with graphene has been performed in the mid-infrared part of the spectrum using a Nicolet 6700 FTIR spectrometer coupled to a Thermo Scientific Continuum microscope with NA = 0.58. The sample spectra averaged over 32 scans were collected with spectral resolution of 4 cm^{-1}.

Best-Fit Procedure for Calculating the Scattering Time of the Free Carriers. The calculation of the scattering time τ was done using a two-parameter best-fit procedure. The fitting parameters are τ and the lifetime of the bare metasurface τ_d. After calculating the frequency of the bare metasurface's resonance ω_d

from a simulation, we used the lifetime τ_d of the bare metasurface as a free parameter and calculated $\Delta\tilde{\omega}_d^n$ from eq 5 for a wide range of carrier densities n. The lhs of eq 6 was expressed as a τ_d-dependent quantity $E(n; \tau_d)$. Next, the rhs of eq 6 was expressed as a τ-dependent quantity $T(n; \tau)$. Graphene conductivities that need to be inserted into the rhs of eq 6 were calculated from eq 3. The best-fit pair (τ, τ_d) was determined by minimizing the difference function $\mathrm{Diff}(n; \tau, \tau_d) = [E(n; \tau_d) - T(n; \tau)]^2$ in MATLAB.

Numerical Simulations. A commercial finite elements solver COMSOL Multiphysics was used for simulations. The SLG was modeled using a surface current[50] $J_{SLG} = \sigma_{SLG} E_t$, where E_t is the tangential electric field on the graphene plane.

■ ASSOCIATED CONTENT

Ⓢ Supporting Information

Further details on the effect of the SiO_2 spacer on the quality factor of the plasmonic mode and the multi-Lorentzian reflectivity fit are provided. This material is available free of charge via the Internet at http://pubs.acs.org.

■ AUTHOR INFORMATION

Corresponding Author

*E-mail: gena@physics.utexas.edu.

Notes

The authors declare no competing financial interest.

■ ACKNOWLEDGMENTS

This work was supported by the Office of Naval Research (ONR) Award N00014-13-1-0837 and by the National Science Foundation (NSF) Award DMR 1120923. I.K., C.M., and R.S.R. would like to acknowledge the support from a Tokyo Electron Ltd. (TEL)-customized Semiconductor Research Corporation Award (2009-OJ-1873) and the Office of Naval Research (Grant N00014-10-1-0254). Babak Fallahazad, Sommayeh Rahimi, and Nima Asoudegi are acknowledged for their advice on the fabrication procedures.

■ REFERENCES

(1) Holloway, C. L.; Kuester, E. F.; Gordon, J. A.; O'Hara, J.; Booth, J.; Smith, D. R. An Overview of the Theory and Applications of Metasurfaces: The Two-Dimensional Equivalents of Metamaterials. *IEEE Antennas Propag. Mag.* **2012**, *54*, 10−35.

(2) Kildishev, A. V.; Boltasseva, A.; Shalaev, V. M. Planar Photonics with Metasurfaces. *Science* **2013**, *339*, 1232009.

(3) Yu, N.; Genevet, P.; Kats, M. A.; Aieta, F.; Tetienne, J.-P.; Capasso, F.; Gaburro, Z. Light Propagation with Phase Discontinuities: Generalized Laws of Reflection and Refraction. *Science* **2011**, *334*, 333−337.

(4) Wu, C.; Khanikaev, A. B.; Shvets, G. Broadband Slow Light Metamaterial Based on a Double-Continuum Fano Resonance. *Phys. Rev. Lett.* **2011**, *106*, 107403.

(5) Spinelli, P.; Verschuuren, M. A.; Polman, A. Broadband Omnidirectional Antireflection Coating Based on Subwavelength Surface Mie Resonators. *Nat. Commun.* **2012**, *3*, 692.

(6) Gansel, J. K.; Thiel, M.; Rill, M. S.; Decker, M.; Bade, K.; Saile, V.; Freymann, G. von; Linden, S.; Wegener, M. Gold Helix Photonic Metamaterial as Broadband Circular Polarizer. *Science* **2009**, *325*, 1513−1515.

(7) Zhao, Y.; Belkin, M. A.; Alù, A. Twisted Optical Metamaterials for Planarized Ultrathin Broadband Circular Polarizers. *Nat. Commun.* **2012**, *3*, 870.

(8) Liu, N.; Tang, M. L.; Hentschel, M.; Giessen, H.; Alivisatos, A. P. Nanoantenna-Enhanced Gas Sensing in a Single Tailored Nanofocus. *Nat. Mater.* **2011**, *10*, 631−636.

(9) Wu, C.; Khanikaev, A. B.; Adato, R.; Arju, N.; Yanik, A. A.; Altug, H.; Shvets, G. Fano-Resonant Asymmetric Metamaterials for Ultrasensitive Spectroscopy and Identification of Molecular Monolayers. *Nat. Mater.* **2011**, *11*, 69−75.

(10) Hao, F.; Sonnefraud, Y.; Dorpe, P. V.; Maier, S. A.; Halas, N. J.; Nordlander, P. Symmetry Breaking in Plasmonic Nanocavities: Subradiant LSPR Sensing and a Tunable Fano Resonance. *Nano Lett.* **2008**, *8*, 3983−3988.

(11) Barth, A.; Zscherp, C. What Vibrations Tell about Proteins. *Q. Rev. Biophys.* **2002**, *35*, 369−430.

(12) Adato, R.; Yanik, A. A.; Amsden, J. J.; Kaplan, D. L.; Omenetto, F. G.; Hong, M. K.; Erramilli, S.; Altug, H. Ultra-Sensitive Vibrational Spectroscopy of Protein Monolayers with Plasmonic Nanoantenna Arrays. *Proc. Natl. Acad. Sci. U.S.A.* **2009**, *106*, 19227−19232.

(13) Zhang, Y.; Wen, F.; Zhen, Y.-R.; Nordlander, P.; Halas, N. J. Coherent Fano Resonances in a Plasmonic Nanocluster Enhance Optical Four-Wave Mixing. *Proc. Natl. Acad. Sci. U.S.A.* **2013**, *110*, 9215−9219.

(14) Klein, M. W.; Enkrich, C.; Wegener, M.; Linden, S. Second-Harmonic Generation from Magnetic Metamaterials. *Science* **2006**, *313*, 502−504.

(15) Liu, X.; Tyler, T.; Starr, T.; Starr, A. F.; Jokerst, N. M.; Padilla, W. J. Taming the Blackbody with Infrared Metamaterials as Selective Thermal Emitters. *Phys. Rev. Lett.* **2011**, *107*, 045901.

(16) Aieta, F.; Genevet, P.; Kats, M. A.; Yu, N.; Blanchard, R.; Gaburro, Z.; Capasso, F. Aberration-Free Ultrathin Flat Lenses and Axicons at Telecom Wavelengths Based on Plasmonic Metasurfaces. *Nano Lett.* **2012**, *12*, 4932−4936.

(17) Memarzadeh, B.; Mosallaei, H. Array of Planar Plasmonic Scatterers Functioning as Light Concentrator. *Opt. Lett.* **2011**, *36*, 2569−2571.

(18) Yu, N.; Aieta, F.; Genevet, P.; Kats, M. A.; Gaburro, Z.; Capasso, F. A Broadband, Background-Free Quarter-Wave Plate Based on Plasmonic Metasurfaces. *Nano Lett.* **2012**, *12*, 6328−6333.

(19) Ni, X.; Emani, N. K.; Kildishev, A. V.; Boltasseva, A.; Shalaev, V. M. Broadband Light Bending with Plasmonic Nanoantennas. *Science* **2012**, *335*, 427−427.

(20) Jones, B. F.; Plassmann, P. Digital Infrared Thermal Imaging of Human Skin. *IEEE Eng. Med. Biol. Mag.* **2002**, *21*, 41−48.

(21) Merlot, S.; Mustilli, A.-C.; Genty, B.; North, H.; Lefebvre, V.; Sotta, B.; Vavasseur, A.; Giraudat, J. Use of Infrared Thermal Imaging to Isolate Arabidopsis Mutants Defective in Stomatal Regulation. *Plant J.* **2002**, *30*, 601−609.

(22) Kosterev, A. A.; Tittel, F. K.; Kohler, R.; Gmachl, C.; Capasso, F.; Sivco, D. L.; Cho, A. Y.; Wehe, S.; Allen, M. G. Thermoelectrically Cooled Quantum-Cascade-Laser-Based Sensor for the Continuous Monitoring of Ambient Atmospheric Carbon Monoxide. *Appl. Opt.* **2002**, *41*, 1169−1173.

(23) Fernandez, D. C.; Bhargava, R.; Hewitt, S. M.; Levin, I. W. Infrared Spectroscopic Imaging for Histopathologic Recognition. *Nat. Biotechnol.* **2005**, *23*, 469−474.

(24) Bekman, H. H. P. T.; van den Heuvel, J. C.; van Putten, F. J. M.; Schleijpen, R. Development of a Mid-Infrared Laser for Study of Infrared Countermeasures Techniques. *Proc. SPIE* **2004**, *5615*, 27−38.

(25) Bauer, C.; Geiser, P.; Burgmeier, J.; Holl, G.; Schade, W. Pulsed Laser Surface Fragmentation and Mid-Infrared Laser Spectroscopy for Remote Detection of Explosives. *Appl. Phys. B: Laser Opt.* **2006**, *85*, 251−256.

(26) Yao, Y.; Hoffman, A. J.; Gmachl, C. F. Mid-Infrared Quantum Cascade Lasers. *Nat. Photonics* **2012**, *6*, 432−439.

(27) Rogalski, A. Recent Progress in Infrared Detector Technologies. *Infrared Phys. Technol.* **2011**, *54*, 136−154.

(28) Gunapala, S. D.; Bandara, S. V.; Liu, J. K.; Mumolo, J. M.; Ting, D. Z.; Hill, C. J.; Nguyen, J.; Simolon, B.; Woolaway, J.; Wang, S. C.; Li, W.; LeVan, P. D.; Tidrow, M. Z. 1024 × 1024 Format Pixel Co-Located Simultaneously Readable Dual-Band QWIP Focal Plane. *Infrared Phys. Technol.* **2009**, *52*, 395−398.

(29) Rogalski, A. Progress in Focal Plane Array Technologies. *Prog. Quantum Electron.* **2012**, *36*, 342−473.

(30) Haus, H. *Waves and Fields in Optoelectronics*; Prentice-Hall: Upper Saddle River, NJ, 1984.

(31) Kossyrev, P. A.; Yin, A.; Cloutier, S. G.; Cardimona, D. A.; Huang, D.; Alsing, P. M.; Xu, J. M. Electric Field Tuning of Plasmonic Response of Nanodot Array in Liquid Crystal Matrix. *Nano Lett.* **2005**, *5*, 1978−1981.

(32) Berthelot, J.; Bouhelier, A.; Huang, C.; Margueritat, J.; Colas-des-Francs, G.; Finot, E.; Weeber, J.-C.; Dereux, A.; Kostcheev, S.; Ahrach, H. I. E.; Baudrion, A.-L.; Plain, J.; Bachelot, R.; Royer, P.; Wiederrecht, G. P. Tuning of an Optical Dimer Nanoantenna by Electrically Controlling Its Load Impedance. *Nano Lett.* **2009**, *9*, 3914−3921.

(33) Xu, G.; Huang, C.-M.; Tazawa, M.; Jin, P.; Chen, D.-M. Nano-Ag on Vanadium Dioxide. II. Thermal Tuning of Surface Plasmon Resonance. *J. Appl. Phys.* **2008**, *104*, 053102.

(34) Huang, F.; Baumberg, J. J. Actively Tuned Plasmons on Elastomerically Driven Au Nanoparticle Dimers. *Nano Lett.* **2010**, *10*, 1787−1792.

(35) Abb, M.; Albella, P.; Aizpurua, J.; Muskens, O. L. All-Optical Control of a Single Plasmonic Nanoantenna−ITO Hybrid. *Nano Lett.* **2011**, *11*, 2457−2463.

(36) Kim, J.; Son, H.; Cho, D. J.; Geng, B.; Regan, W.; Shi, S.; Kim, K.; Zettl, A.; Shen, Y.-R.; Wang, F. Electrical Control of Optical Plasmon Resonance with Graphene. *Nano Lett.* **2012**, *12*, 5598−5602.

(37) Majumdar, A.; Kim, J.; Vuckovic, J.; Wang, F. Electrical Control of Silicon Photonic Crystal Cavity by Graphene. *Nano Lett.* **2013**, *13*, 515−518.

(38) Jun, Y. C.; Gonzales, E.; Reno, J. L.; Shaner, E. A.; Gabbay, A.; Brener, I. Active Tuning of Mid-Infrared Metamaterials by Electrical Control of Carrier Densities. *Opt. Express* **2012**, *20*, 1903−1911.

(39) Tang, L.; Kocabas, S. E.; Latif, S.; Okyay, A. K.; Ly-Gagnon, D.-S.; Saraswat, K. C.; Miller, D. A. B. Nanometre-Scale Germanium Photodetector Enhanced by a near-Infrared Dipole Antenna. *Nat. Photonics* **2008**, *2*, 226−229.

(40) Ooi, K. J. A.; Bai, P.; Chu, H. S.; Ang, L. K. Vandium Dioxide Active Plasmonics. Photonics Global Conference (PGC), Nanyang Technological University Singapore, Singapore, Dec 13−16, 2012, Curran Associates: Red Hook, NY, 2012; pp 1−4.

(41) Bai, P.; Gu, M.-X.; Wei, X.-C.; Li, E.-P. Electrical Detection of Plasmonic Waves Using an Ultra-Compact Structure via a Nanocavity. *Opt. Express* **2009**, *17*, 24349−24357.

(42) Stewart, M. E.; Anderton, C. R.; Thompson, L. B.; Maria, J.; Gray, S. K.; Rogers, J. A.; Nuzzo, R. G. Nanostructured Plasmonic Sensors. *Chem. Rev.* **2008**, *108*, 494−521.

(43) Anker, J. N.; Hall, W. P.; Lyandres, O.; Shah, N. C.; Zhao, J.; Van Duyne, R. P. Biosensing with Plasmonic Nanosensors. *Nat. Mater.* **2008**, *7*, 442−453.

(44) Liu, N.; Mesch, M.; Weiss, T.; Hentschel, M.; Giessen, H. Infrared Perfect Absorber and Its Application As Plasmonic Sensor. *Nano Lett.* **2010**, *10*, 2342−2348.

(45) Lu, Y.-J.; Kim, J.; Chen, H.-Y.; Wu, C.; Dabidian, N.; Sanders, C. E.; Wang, C.-Y.; Lu, M.-Y.; Li, B.-H.; Qiu, X.; Chang, W.-H.; Chen, L.-J.; Shvets, G.; Shih, C.-K.; Gwo, S. Plasmonic Nanolaser Using Epitaxially Grown Silver Film. *Science* **2012**, *337*, 450−453.

(46) Liu, X.; Starr, T.; Starr, A. F.; Padilla, W. J. Infrared Spatial and Frequency Selective Metamaterial with Near-Unity Absorbance. *Phys. Rev. Lett.* **2010**, *104*, 207403.

(47) Rizzo, G.; Bettarini, S.; Calderini, G.; Cenci, R.; Forti, F.; Giorgi, M. A.; Morsani, F.; Ratti, L.; Speziali, V.; Manghisoni, M.; Re, V.; Traversi, G.; Bosisio, L. A Novel Monolithic Active Pixel Detector in Triple Well CMOS Technology with Pixel Level Analog Processing. *Nucl. Instrum. Methods Phys. Res., Sect. A* **2006**, *565*, 195−201.

(48) Sun, B.; Edgar, M. P.; Bowman, R.; Vittert, L. E.; Welsh, S.; Bowman, A.; Padgett, M. J. 3D Computational Imaging with Single-Pixel Detectors. *Science* **2013**, *340*, 844−847.

(49) Papasimakis, N.; Luo, Z.; Shen, Z. X.; De Angelis, F.; Di Fabrizio, E.; Nikolaenko, A. E.; Zheludev, N. I. Graphene in a Photonic Metamaterial. *Opt. Express* **2010**, *18*, 8353−8359.

(50) Mousavi, S. H.; Kholmanov, I.; Alici, K. B.; Purtseladze, D.; Arju, N.; Tatar, K.; Fozdar, D. Y.; Suk, J. W.; Hao, Y.; Khanikaev, A. B.; Ruoff, R. S.; Shvets, G. Inductive Tuning of Fano-Resonant Metasurfaces Using Plasmonic Response of Graphene in the Mid-Infrared. *Nano Lett.* **2013**, *13*, 1111−1117.

(51) Yao, Y.; Kats, M. A.; Genevet, P.; Yu, N.; Song, Y.; Kong, J.; Capasso, F. Broad Electrical Tuning of Graphene-Loaded Plasmonic Antennas. *Nano Lett.* **2013**, *13*, 1257−1264.

(52) Emani, N. K.; Chung, T.-F.; Ni, X.; Kildishev, A. V.; Chen, Y. P.; Boltasseva, A. Electrically Tunable Damping of Plasmonic Resonances with Graphene. *Nano Lett.* **2012**, *12*, 5202−5206.

(53) Emani, N. K.; Chung, T.-F.; Kildishev, A. V.; Shalaev, V. M.; Chen, Y. P.; Boltasseva, A. Electrical Modulation of Fano Resonance in Plasmonic Nanostructures Using Graphene. *Nano Lett.* **2014**, *14*, 78−82.

(54) Li, Z.; Yu, N. Modulation of Mid-Infrared Light Using Graphene-Metal Plasmonic Antennas. *Appl. Phys. Lett.* **2013**, *102*, 131108.

(55) Yao, Y.; Kats, M. A.; Shankar, R.; Song, Y.; Kong, J.; Loncar, M.; Capasso, F. Wide Wavelength Tuning of Optical Antennas on Graphene with Nanosecond Response Time. *Nano Lett.* **2014**, *14*, 214−219.

(56) Chu, H.-S.; How Gan, C. Active Plasmonic Switching at Mid-Infrared Wavelengths with Graphene Ribbon Arrays. *Appl. Phys. Lett.* **2013**, *102*, 231107.

(57) Wang, F.; Shen, Y. R. General Properties of Local Plasmons in Metal Nanostructures. *Phys. Rev. Lett.* **2006**, *97*, 206806.

(58) Zhang, S.; Genov, D. A.; Wang, Y.; Liu, M.; Zhang, X. Plasmon-Induced Transparency in Metamaterials. *Phys. Rev. Lett.* **2008**, *101*, 047401.

(59) Khanikaev, A. B.; Mousavi, S. H.; Wu, C.; Dabidian, N.; Alici, K. B.; Shvets, G. Electromagnetically Induced Polarization Conversion. *Opt. Commun.* **2012**, *285*, 3423−3427.

(60) Adato, R.; Yanik, A. A.; Altug, H. On Chip Plasmonic Monopole Nano-Antennas and Circuits. *Nano Lett.* **2011**, *11*, 5219−5226.

(61) Pendry, J. B.; Holden, A. J.; Robbins, D. J.; Stewart, W. J. Low Frequency Plasmons in Thin-Wire Structures. *J. Phys.: Condens. Matter* **1998**, *10*, 4785.

(62) Brar, V. W.; Jang, M. S.; Sherrott, M.; Lopez, J. J.; Atwater, H. A. Highly Confined Tunable Mid-Infrared Plasmonics in Graphene Nanoresonators. *Nano Lett.* **2013**, *13*, 2541−2547.

(63) Chen, D.-Z. A.; Chen, G. Measurement of Silicon Dioxide Surface Phonon-Polariton Propagation Length by Attenuated Total Reflection. *Appl. Phys. Lett.* **2007**, *91*, 121906.

(64) Fano, U. Effects of Configuration Interaction on Intensities and Phase Shifts. *Phys. Rev.* **1961**, *124*, 1866−1878.

(65) Artar, A.; Yanik, A. A.; Altug, H. Multispectral Plasmon Induced Transparency in Coupled Meta-Atoms. *Nano Lett.* **2011**, *11*, 1685−1689.

(66) Khanikaev, A. B.; Wu, C.; Shvets, G. Fano-Resonant Metamaterials and Their Applications. *Nanophotonics* **2013**, *2*, 247−264.

(67) Novoselov, K. S.; Geim, A. K.; Morozov, S. V.; Jiang, D.; Katsnelson, M. I.; Grigorieva, I. V.; Dubonos, S. V.; Firsov, A. A. Two-Dimensional Gas of Massless Dirac Fermions in Graphene. *Nature* **2005**, *438*, 197−200.

(68) Cai, W.; White, J. S.; Brongersma, M. L. Compact, High-Speed and Power-Efficient Electrooptic Plasmonic Modulators. *Nano Lett.* **2009**, *9*, 4403−4411.

(69) Barrios, C. A.; de Almeida, V. R.; Lipson, M. Low-Power-Consumption Short-Length and High-Modulation-Depth Silicon Electrooptic Modulator. *J. Lightwave Technol.* **2003**, *21*, 1089−1098.

(70) Vassant, S.; Archambault, A.; Marquier, F.; Pardo, F.; Gennser, U.; Cavanna, A.; Pelouard, J. L.; Greffet, J. J. Epsilon-Near-Zero Mode for Active Optoelectronic Devices. *Phys. Rev. Lett.* **2012**, *109*, 237401.

(71) Palik, E. *Handbook of Optical Constants of Solids*; Academic Press: New York, 1997.

(72) Larouche, S.; Tsai, Y.-J.; Tyler, T.; Jokerst, N. M.; Smith, D. R. Infrared Metamaterial Phase Holograms. *Nat. Mater.* **2012**, *11*, 450−454.

(73) Kim, S.; Nah, J.; Jo, I.; Shahrjerdi, D.; Colombo, L.; Yao, Z.; Tutuc, E.; Banerjee, S. K. Realization of a High Mobility Dual-Gated Graphene

Field-Effect Transistor with Al_2O_3 Dielectric. *Appl Phys. Lett.* **2009**, *94*, 062107.

(74) Adam, S.; Hwang, E. H.; Galitski, V. M.; Sarma, S. D. A Self-Consistent Theory for Graphene Transport. *Proc. Natl. Acad. Sci. U.S.A.* **2007**, *104*, 18392−18397.

(75) Fei, Z.; Rodin, A. S.; Andreev, G. O.; Bao, W.; McLeod, A. S.; Wagner, M.; Zhang, L. M.; Zhao, Z.; Thiemens, M.; Dominguez, G.; Fogler, M. M.; Neto, A. H. C.; Lau, C. N.; Keilmann, F.; Basov, D. N. Gate-Tuning of Graphene Plasmons Revealed by Infrared Nano-Imaging. *Nature* **2012**, *487*, 82−85.

(76) Horng, J.; Chen, C.-F.; Geng, B.; Girit, C.; Zhang, Y.; Hao, Z.; Bechtel, H. A.; Martin, M.; Zettl, A.; Crommie, M. F.; Shen, Y. R.; Wang, F. Drude Conductivity of Dirac Fermions in Graphene. *Phys. Rev. B* **2011**, *83*, 165113.

(77) Li, X.; Zhu, Y.; Cai, W.; Borysiak, M.; Han, B.; Chen, D.; Piner, R. D.; Colombo, L.; Ruoff, R. S. Transfer of Large-Area Graphene Films for High-Performance Transparent Conductive Electrodes. *Nano Lett.* **2009**, *9*, 4359−4363.

(78) Kholmanov, I. N.; Magnuson, C. W.; Aliev, A. E.; Li, H.; Zhang, B.; Suk, J. W.; Zhang, L. L.; Peng, E.; Mousavi, S. H.; Khanikaev, A. B.; Piner, R.; Shvets, G.; Ruoff, R. S. Improved Electrical Conductivity of Graphene Films Integrated with Metal Nanowires. *Nano Lett.* **2012**, *12*, 5679−5683.

(79) Falkovsky, L. A.; Pershoguba, S. S. Optical Far-Infrared Properties of a Graphene Monolayer and Multilayer. *Phys. Rev. B* **2007**, *76*, 153410.